The Astrophysical Journal, 719:151–165, 2010 August 10 doi:10.1088/0004-637X/719/1/151

FROM LARGE-SCALE LOOPS TO THE SITES OF DENSE FLARING LOOPS: PREFERENTIAL CONDITIONS FOR LONG-PERIOD PULSATIONS IN SOLAR FLARES

C. Foullon[1], L. Fletcher[2], I. G. Hannah[2], E. Verwichte[1], B. Cecconi[3], V. M. Nakariakov[1], K. J. H. Phillips[4], and B. L. Tan[5]

[1] Centre for Fusion, Space and Astrophysics, Department of Physics, University of Warwick, Coventry CV4 7AL, UK; claire.foullon@warwick.ac.uk
[2] Department of Physics and Astronomy, University of Glasgow, Glasgow G12 8QQ, UK
[3] LESIA, CNRS, UPMC, Université Paris Diderot, Observatoire de Paris, 5 Place Jules Janssen, 92190 Meudon, France
[4] Mullard Space Science Laboratory, University College London, Holmbury St Mary, Dorking, Surrey RH5 6NT, UK
[5] Key Laboratory of Solar Activity, National Astronomical Observatories of Chinese Academy of Sciences, Beijing 100012, China
Received 2010 April 14; accepted 2010 June 5; published 2010 July 19

ABSTRACT

Long-period quasi-periodic pulsations (QPPs) of solar flares are a class apart from shorter period events. By involving an external resonator, the mechanism they call upon differs from traditional QPP models, but has wider applications. We present a multi-wavelength analysis of spatially resolved QPPs, with periods around 10 minutes, observed in the X-ray spectrum primarily at energies between 3 and 25 keV. Complementary observations obtained in Hα and radio emission in the kHz to GHz frequency range, together with an analysis of the X-ray plasma properties provide a comprehensive picture that is consistent with a dense flaring loop subject to periodic energization and thermalization. The QPPs obtained in Hα and type III radio bursts, with similar periods as the QPPs in soft X-rays, have the longest periods ever reported for those types of data sets. We also report 1–2 GHz radio emission, concurrent with but unrestricted to the QPP time intervals, which is multi-structured at regularly separated narrowband frequencies and modulated with ∼18 minute periods. This radio emission can be attributed to the presence of multiple "quiet" large-scale loops in the background corona. Large scale but shorter inner loops below may act as preferential resonators for the QPPs. The observations support interpretations consistent with both inner and outer loops subject to fast kink magnetohydrodynamic waves. Finally, X-ray imaging indicates the presence of double coronal sources in the flaring sites, which could be the particular signatures of the magnetically linked inner loops. We discuss the preferential conditions and the driving mechanisms causing the repeated flaring.

Key words: Sun: corona – Sun: flares – Sun: oscillations – Sun: particle emission – Sun: radio radiation – Sun: X-rays, gamma rays

Online-only material: color figures

1. INTRODUCTION

Quasi-periodic pulsations (QPPs) of solar flaring emission, with periods from tenths of seconds to several minutes, have been detected since the early 1970s at wavelengths covering a wide frequency band from radio waves to hard X-rays (Aschwanden 2004) and, as shown recently, in gamma-rays (Nakariakov et al. 2010). Solar flares radiate over a wide range of wavelengths, corresponding to different emission mechanisms and originating from different spatial positions. Thus, in order to establish a comprehensive picture of the processes at work, it is essential to study flares and their QPPs across the entire electromagnetic spectrum.

The advent of the *Reuven Ramaty High Energy Solar Spectroscopic Imager* (*RHESSI*) has allowed X-ray investigations of QPPs with high spatial and temporal resolution (Foullon et al. 2005; Li & Gan 2008; Zimovets & Struminsky 2009, 2010; Nakariakov et al. 2010). Combining this opportunity with complementary data at other wavelengths, Foullon et al. (2005), hereinafter referred to as F05, suggested that observed QPPs, with periods around 10 minutes, could be explained as modulations in the emission from a small flaring loop due to kink magnetohydrodynamic (MHD) waves in a magnetically linked and large-scale coronal loop (acting as a long-period resonator). This study introduced long-period QPPs with periods of several minutes as a class apart from other shorter period events. By involving an external resonator, the mechanism they call upon differs from traditional QPP models, but has wider applications.

This proposed mechanism still explains long-period QPPs in terms of MHD waves and oscillations (Roberts et al. 1983, 1984) that, independently, are directly observed in solar coronal structures. The MHD kink oscillation has been widely exploited in recent years through MHD coronal seismology (e.g., Nakariakov et al. 1999). Dynamic events, such as flares, prominence eruptions, or coronal mass ejections (CMEs), often excite resonant kink modes of MHD waves in neighboring coronal structures. The majority of the observational studies have been made by imaging instruments in the EUV (1–1.6 MK), notably by the *Transition Region And Coronal Explorer* (*TRACE*). Oscillations with similar 10 minute periods have been detected in coronal green line emission (Fe XIV 5303 Å, 2 MK) by the Doppler coronagraph NOGIS (Norikura Green-line Imaging System, Japan; Hori et al. 2005). They were subsequently shown to occur in a bundle of face-on loops, not synchronized in phase, but with periods increasing with height (up to 15.3 minutes), and could be interpreted as MHD fast kink oscillations (Hori et al. 2007). Recently, similar kink oscillations (with a period of 10.5 minutes) were observed in a large-scale loop with the twin *Solar TErrestrial RElations Observatory* (*STEREO*) spacecraft (Verwichte et al. 2009), and the kink oscillations of a whole coronal arcade were detected with the *SOlar and Heliospheric*

Table 1
Observing Instruments, the Data used (Frequency of Wavelength), their Spatial or Spectral Resolution, and their Temporal Resolution (or Most Regular Cadence)

Reference	Instrument	Frequency of Wavelength	Spatial/Frequency Resolution	Time Cadence
1	*RHESSI*	3–25 keV	0.5 pixel arcsec^{-1}	4.1 s
2	XRS/GOES-8	1–8 Å, 0.5–4 Å	...	3 s
3	BBSO	Hα (6563 Å)	1.06 pixel arcsec^{-1}	60 s
4	SOON Learmonth	Hα (6563 Å)	0.75 pixel arcsec^{-1}	30 s
5	HSOS	Hα (6563 Å)	1.05 pixel arcsec^{-1}	10–11 s
6	WAVES/*Wind*	30–1000 kHz	3 kHz	60 s
7	URAP/*Ulysses*	30–940 kHz	3 kHz	144 s
8	OVSA	1.2–2.4 GHz	200 MHz	8 s
9	SBRS	1–2 GHz	4 MHz	0.2 s
10	NoRH	17 GHz	4.91 pixel arcsec^{-1}	1 s

References. (1) Lin et al. 2002; (2) Hanser & Sellers 1996; (3) Denker et al. 1999; (4) Coffey & Lincoln 1979; Kiplinger 1998; (5) Ai & Hu 1986; (6) Bougeret et al. 1995; (7) Stone et al. 1992; (8) Hurford et al. 1984; Gary & Hurford 1990; (9) Fu et al. 1995, 2004; (10) Nakajima et al. 1994.

Observatory (*SOHO*), at the largest periods ever reported (increasing with height from 24 up to 180 minutes; Verwichte et al. 2010).

By linking together solar flare pulsations and MHD kink oscillations, the observations by F05 with *RHESSI* have encouraged new theoretical avenues, e.g., explaining the "coupling" or "interaction" between the loop oscillations and the flaring loop emission (Nakariakov et al. 2006). It must be stressed that the mechanism proposed by F05 was supported by observational evidence in soft X-rays and by the presence of a transequatorial loop (TEL) connecting two active regions. The role of a nearby, adequately long, loop in similar hard X-ray observations of QPPs by Li & Gan (2008), but with somewhat shorter (4 minutes) periods, could not be assessed with the available temporal resolution of imaging instruments in the extreme-UV. Moreover, several examples of long-period QPPs in soft X-rays exist for single active regions on the disk, pointing to another scenario, though in such cases, a long loop may be below instrument detectability.

Of particular interest is the detection of current sheets and their relevance for the formation of "plasmoids" above flare loops (e.g., Ohyama & Shibata 1998; Sui et al. 2005). We refer to a plasmoid comprehensively as either a closed (magnetic island) or helical (flux rope) magnetic field structure. Upward or downward motions of the plasmoids can be inferred from, respectively, negative or positive frequency drifts of pulsating structures observed in the radio decimetric (0.3–3 GHz) frequency range (e.g., Kliem et al. 2000; Khan et al. 2002). Further evidence of plasmoid motion is found in white light coronagraph images and in X-ray (*RHESSI*) images (e.g., Milligan et al. 2010 and references therein). While plasmoid ejection is consistent with the flare model of an upwardly moving magnetic flux rope, below which the reconnecting current sheet is formed (e.g., Karlický 2004; Lehtinen et al. 2005), downward moving plasmoids interacting with the flare loop arcade below may result in plasmoid coalescence (e.g., Kołomański & Karlický 2007; Milligan et al. 2010). Plasmoid formation in pre-existing current sheets may result from the tearing and coalescence instabilities in the regime of dynamic magnetic reconnection (Kliem et al. 2000) or from Alfvénic shear flows leading to the onset of the Kelvin–Helmholtz instability and to overstable oscillating modes (Ofman & Sui 2006). Under typical coronal conditions, those models appear designed to explain QPPs of relatively short periods and in hard X-rays. Whether they can explain long-period QPPs in soft X-rays is a question that remains to be addressed.

In order to understand the physical processes at work in the flaring loops and their surrounding coronal environment, we extend the analysis of the QPPs of 2003 February 5 and 6, reported by F05 in different X-ray wavelengths, with observations in Hα and radio emission. After introducing the observations in Section 2, a comparative study of one QPP sequence across the energy spectrum is carried out in Section 3 and additional coronal oscillations in 1–2 GHz radio spectra are presented and discussed in Section 4. Section 5 discusses the likely scenario to explain the derived properties of those long-period QPPs.

2. OBSERVATIONS

2.1. Events

Table 1 lists the observing instruments used in this study and their temporal resolution or most regular cadence. The flaring activity of 2003 February 5 and 6 displays two QPP sequences, seen well in X-rays between 3 and 25 keV. Full disk X-ray measurements with the X-ray Sensor (XRS) aboard the *Geostationary Operational Environmental Satellite* (*GOES*)-8 and with the *RHESSI* experiment are shown in panels (a) and (b) of Figure 1. The first QPP sequence on February 5, denoted "QPP1," is associated with two flares: as seen by *GOES*, the first flare of class C2.1 peaks at 20:37 UT and the second flare of class C2.2 at 21:39 UT. Less than 5 hr later, the second sequence on February 6, denoted "QPP2," follows a C3.4 flare peaking at 2:12 UT.

Each cyclic event or pulsation in a QPP sequence is denoted alphabetically, as shown near the top of Figure 1. Table 2 lists the flare events as reported in edited solar event lists by NOAA and *RHESSI*. In QPP1, besides the two flares corresponding to events (1a) and (1e) seen both by *GOES* and *RHESSI*, the pulsations in X-rays observed by *RHESSI* are also classified as flares. In QPP2, flare (2a) seen by *GOES* and *RHESSI* is accompanied by a fixed-frequency radio burst. The following pulsation (2b) in X-rays is classified as a flare by *RHESSI* and is followed by two Hα brightenings (2b) and (2d) classified as subflares. In Figure 1(b), note that between (2a) and (2b), the high energy (>12 keV) peak at 02:18 UT in *RHESSI* is attributed to particle emission from the satellite's in situ environment.

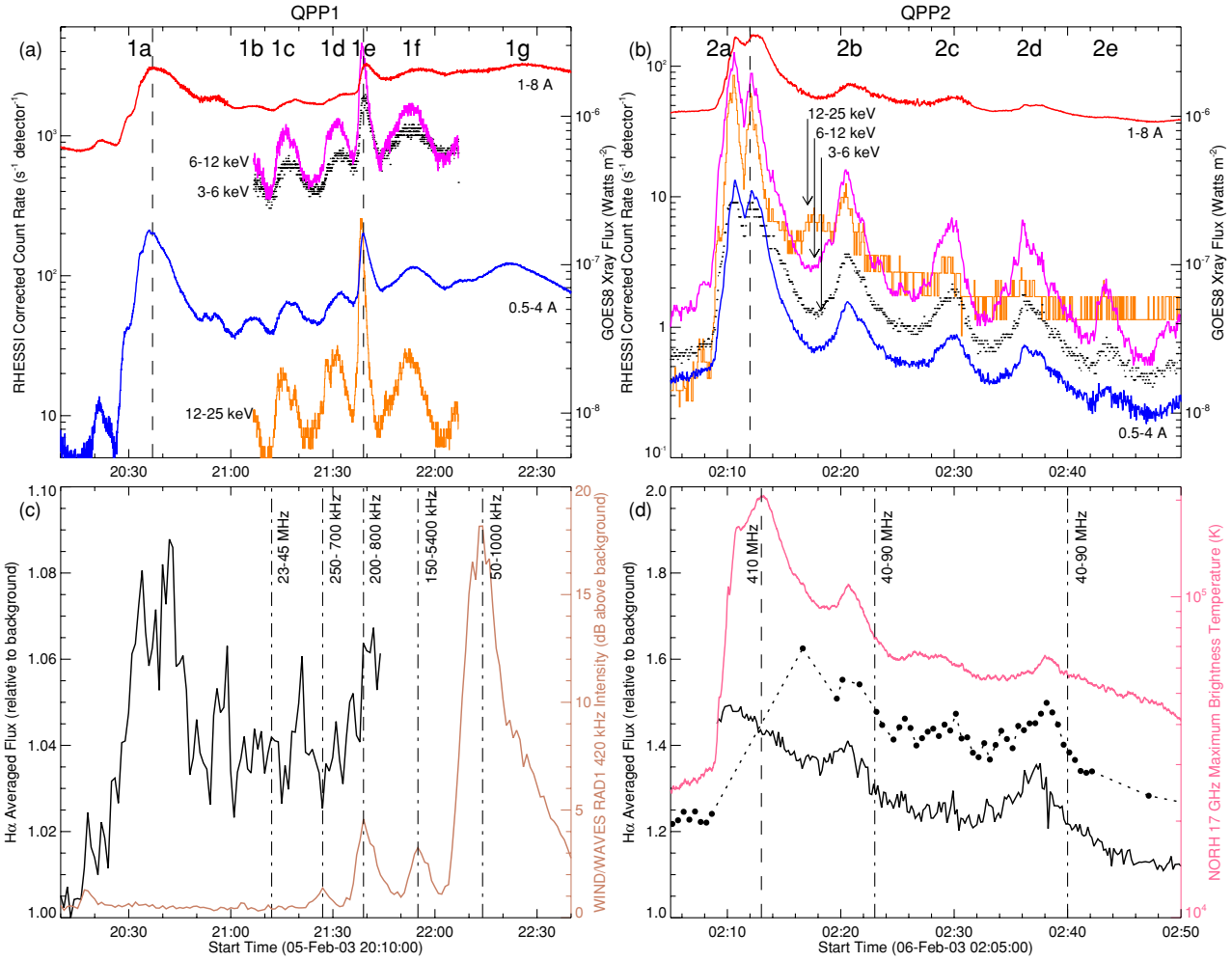

Figure 1. (a) and (b) Full disk measurements in X-rays from GOES-8 (1–8 Å and 0.5–4 Å) and *RHESSI* (3–6 keV, 6–12 keV, and 12–25 keV). The vertical dashed lines indicate the peak times of the flares, as seen by *GOES* 1–8 Å. (c) and (d) Hα and radio observations. The Hα flux, averaged in the corresponding flaring region (relative to background), is shown (as solid lines) with data from (c) BBSO, (d) HSOS, and (as full circles joined by a dotted line) SOON Learmonth. Vertical dot-dashed lines indicate type III radio bursts observed in the annotated frequency range; the vertical dashed line in panel (d) indicates a fixed-frequency radio burst at 410 MHz reported both at Learmonth and Palehua. The colored solid lines with corresponding *y*-axes on the right show (c) (brown) the radio intensity at the fixed frequency of 420 kHz from RAD1/WAVES/*Wind*, corresponding to low-frequency type III radio bursts, and (d) (magenta) the radio brightness temperature at 17 GHz, averaged in region A, from NoRH.

(A color version of this figure is available in the online journal.)

Using imaging data from *RHESSI*, F05 showed that each QPP sequence originates mainly from a single site, which corresponds to the site of the associated flare(s): QPP1 originates from NOAA Active Region 10278 in the northern hemisphere (referred to as region B), while QPP2 originates from NOAA Active Region 10277, oppositely located across the solar equator, in the southern hemisphere (referred to as region A); see panels (c) and (d) of Figure 2. The exception to this is the pulsation (2e), seen to originate from region B, rather than region A (F05, their Figure 1(d)).

In order to present a picture of the QPP that is as complete as possible, we next describe observations in Hα and radio wavelengths as well as additional X-ray *RHESSI* imaging and spectral observations. Some Hα and radio observations are presented in panels (c) and (d) of Figure 1 for QPP1 and QPP2, respectively.

2.2. Hα Observations

Available Hα images come from three stations: the Big Bear Solar Observatory (BBSO), U.S.; the Huairou Solar Observatory Station (HSOS), China; and the Solar Optical Observing Network (SOON) Learmonth Observatory, Australia. The data sets come with different fields of view (FOVs), which do not necessarily include the limb. Full-disk FOVs are available with the BBSO data set (and one of two HSOS data sets, with lower spatial resolution, not used here). Within each data set, the images are co-aligned (using cross-correlation). This treatment is sufficient for the purpose of averaging the intensity in given regions of interest (ROIs). In order to obtain absolute positions, as presented in panels (a) and (b) of Figure 2, a geometric registration is performed between salient points in a reference image and the Hα image of interest, followed by affine transformations to calculate relative scaling, rotation, and displacement. In panel (a), the BBSO image has been registered with a full-disk magnetogram image (from *SOHO*/MDI); in panel (b), the Learmonth image was registered with a correctly positioned BBSO image.

Although the time resolution of available Hα imaging sequences of the chromosphere is much finer than the QPP periodicities, their quality and spatial resolution are not sufficient to give accurate descriptions on the topological connectivities of

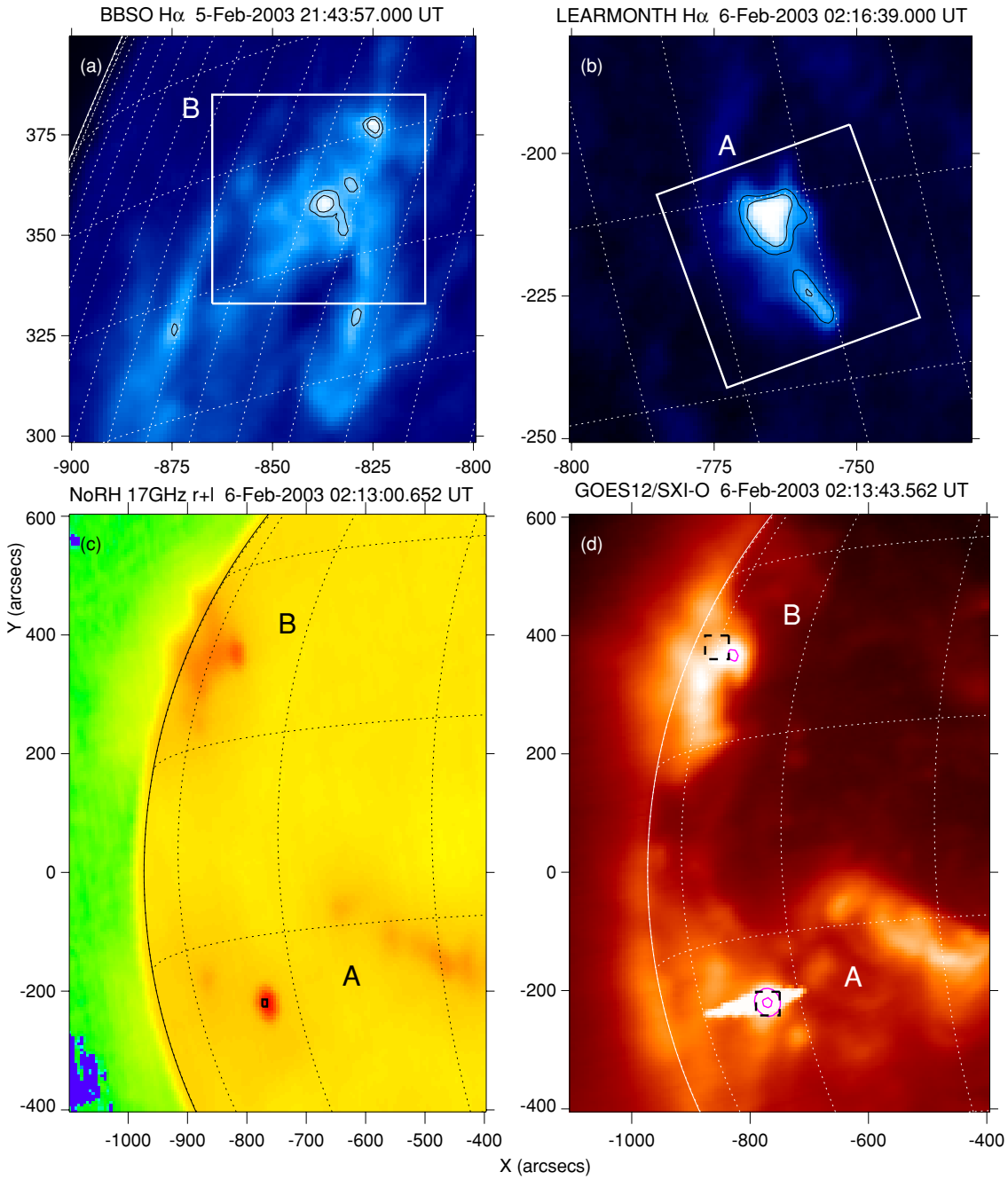

Figure 2. (a) and (b) Hα images centered on the source regions, taken from (a) BBSO at time of QPP1 and (b) Learmonth at time of QPP2; an ROI is overlaid in white. (c) and (d) East limb images taken at the time of the flare on 2003 February 6 at 2:13:00 UT showing both NOAA Active Region 10278 in the northern hemisphere (region B, producing QPP1) and NOAA Active Region 10277, oppositely located across the solar equator, in the southern hemisphere (region A, producing QPP2): (c) NoRH 17 GHz image, with overlaid ROI, corresponding to the source region A, where the maximum is taken in Figure 1(d), and (d) GOES-12/Soft X-ray Imager (SXI) image (open filter) with overlaid contour levels of a 5–12 keV *RHESSI* image (reconstructed from collimators 5F–9F in the time range 02:05–02:10 UT) shown in pink solid lines (at 20% and 80% of the maximum value); the black dashed boxes are FOVs used in Figure 5. Latitude and longitude grids are overlaid with grid spacings of (a and b) 2° and (c and d) 20°.

(A color version of this figure is available in the online journal.)

the flaring events. However, averaging the Hα data in the ROIs shows that the chromospheric response produces variations in emission, or brightening, reminiscent of the QPP in X-ray emission. The spatial extent of the Hα radiation, indicated by ribbons of light areas in panels (a) and (b), differs markedly between the two active regions. The flare energy, thermal or nonthermal, eventually gets reprocessed and radiated in Hα emission with a time delay determined by the chromosphere and the spatial extent of the ribbons. To give some indication of integrated energy input, while retaining the QPP component of the energy deposited, the BBSO imaging data available during QPP1 are spatially averaged in the ROI overlaid in panel (a). The time series obtained is shown relative to its minimum level in panel (c) of Figure 1. In contrast, during QPP2, where simultaneous observations from HSOS and SOON Learmonth are available, the dominant flaring active region A and its associated chromospheric response are less extended (see Figure 2(b)). Thus, for best correlation with the X-ray QPP2, the Hα flux is spatially

Table 2
Characteristics of Flares Associated with QPPs on 2003 February 5–6, as Reported in Edited Solar Events Lists

Event	Data Type	Begin	Max	End	Duration (minutes:s)	Peak	Integrated	NOAA AR	Source
1a	X-rays 1–8 Å	20:26	20:37	20:49	23	C2.1	2.2E-03		GOES-8
1a	X-rays 12–25 keV	20:27:00	A20:28:22	A20:30:48	>3:48	>18	>14842	10278	*RHESSI*
1b	X-rays 12–25 keV	B21:06:40	B21:06:42	21:08:36	>1:56	>11	>6264	10278	*RHESSI*
1c	X-rays 12–25 keV	21:13:00	21:14:42	21:20:08	7:08	22	38215	10278	*RHESSI*
1d	X-rays 12–25 keV	21:27:32	21:29:50	21:30:00	2:28	30	19280	10278	*RHESSI*
1e	X-rays 1–8 Å	21:35	21:39	21:44	9	C2.2	1.0E-03		GOES-8
1e	X-rays 12–25 keV[a]	21:36:28	21:38:10	21:41:44	5:16	256	156648	10278	*RHESSI*
1f	X-rays 12–25 keV	21:49:32	21:51:14	21:55:24	5:52	30	50208	10278	*RHESSI*
1g	X-rays 12–25 keV	22:04:48	A22:06:34	A22:06:56	>2:08	>23	>13387	10278	*RHESSI*
2a	X-rays 1–8 Å	02:07	02:12	02:14	7	C3.4	1.0E-03		GOES-8
2a	X-rays 12–25 keV[a]	02:09:36	02:10:34	02:14:32	5:56	85	48929	10277	*RHESSI*
2a	Radio 410 MHz	02:13	02:13	02:13	...	67			Palehua
2a	Radio 410 MHz	02:13	02:13	02:13	...	62			Learmonth
2b	X-rays 12–25 keV	02:20:00	02:20:30	02:20:44	0:44	13	2590	10277	*RHESSI*
2b	Hα	B02:24	02:24	02:33	>9	SF ERU		10277	Learmonth
2d	Hα	02:34	02:39	02:42	8	SF		10277	Learmonth

Notes. The solar reports are edited by NOAA (National Geophysical Data Center or Space Environment Center) and the flare list of *RHESSI*. Letters "A" (after) and "B" (before) were used to indicate later or earlier times, in particular where *RHESSI* flares were interrupted by the *RHESSI* orbit night. The importance of each event is indicated by particulars of the data at "peak" time and "integrated" over the flare duration. For X-ray flares observed with *GOES* (1–8 Å), these correspond to the peak flux (*GOES* class) and the integrated flux (Joules m^{-2}). For X-ray flares observed with *RHESSI* (12–25 keV), these are the peak rate (counts s^{-1}) and total counts. For a fixed-frequency radio burst, the peak value above pre-burst background is given (1 flux unit = 10^{-22} Wm^{-2} Hz^{-1}). For optical Hα flares, S is for subflare (area at maximum brightness $\leqslant$2.0 heliospheric square degrees), F is for faint relative maximum brightness, and ERU indicates several eruptive centers.

[a] The highest energy band in which the flare was observed is 25–50 keV.

averaged over a smaller ROI and above a certain threshold. In an HSOS image at time t, for a given ROI from region A (with intensity values I), a dynamic threshold level of 50% is chosen, i.e., min(I) + 50% (max(I)–min(I)). In the Learmonth imaging sequence of the ROI (represented in Figure 2(b)), a fixed threshold value of 1.1 flux units (close to a corresponding 60% dynamic threshold) is taken. The image sequences from HSOS and SOON Learmonth suffer from much intensity variations with time, due to instrumental or atmospheric effects. The Hα flux time series shown in panel (d) of Figure 1 are therefore both taken relative to a time-varying background flux, which is spatially averaged in a quiet region of the original image FOV. The time series obtained, from simultaneous observations by HSOS and Learmonth, shows common and correlated brightening features, which can therefore be distinguished from noise of non-solar origin. Reports by Learmonth classify the Hα brightenings (2b) and (2d) in QPP2 as two faint subflares. However, what the temporal behavior obtained for these flares essentially suggests is that the chromospheric brightening exceeds both a brightness and an area threshold for more than 18 minutes (starting earlier than 02:24 UT until 02:42 UT) except for 1 minute (02:33–02:34 UT), where it falls below the area threshold (see Table 2).

We thus extract QPPs in Hα data sets. Those QPPs have the longest periods ($\sim$10 minutes) ever observed in Hα, similar to those seen in soft X-rays. As expected, there are no Hα brightening in region A associated with the pulsation (2e) originating from region B.

2.3. Radio Observations

2.3.1. Interplanetary Type III Bursts

Radio type III bursts are generated when suprathermal electrons (with velocity $\sim$0.05–0.3 c, where c is the speed of light) are ejected from solar active regions and then propagate outward along open magnetic field lines through the corona and interplanetary medium. Along their paths these electrons excite Langmuir waves at the local electron plasma frequency, f_{pe}; these electrostatic waves are then partially converted into radio waves at the fundamental or harmonic of f_{pe}. The progress of the electrons into regions of decreasing density produces radio waves progressing to successively lower frequencies.

For the case under study, high-frequency radio events are reported by ground-based stations (Culgoora and Learmonth, Australia and Palehua, Hawaii) and low-frequency type III bursts (in the range from 30 to 5400 kHz) are observed in dynamic spectra from the radio experiment WAVES aboard *Wind* (near the L1 Lagrangian point) and from the Unified Radio and Plasma (URAP) experiment aboard *Ulysses*. The type III frequencies listed in Table 3 correspond to electron densities of about 10^7–10^8 cm^{-3}. The dynamic spectra in Figure 3 are plots of the radio emission intensity observed by *Wind* and *Ulysses* as a function of frequency and time, covering a time interval including the QPP events in X-rays. The most intense of the low-frequency bursts at *Wind*, detected at $\sim$22:24 UT at 420 kHz, has a similar profile as a type III burst detected at *Ulysses* about 22 minutes later ($\sim$22:46 UT at 420 kHz, with a frequency drift of $\sim$30–940 kHz). At that time, *Ulysses* is located 4.6 AU from the Sun, 28° north of the ecliptic plane, and 17° from the Sun–Earth line to the West. Assuming the same radio source for the two burst observations, one can determine its trajectory by triangulation without assuming a density model of the heliosphere (Reiner et al. 1998). While this will not be attempted here, we note qualitatively different frequency drift rates as in the work by Reiner et al. (1998), where the intensity profiles drift more rapidly at *Wind* than at *Ulysses*. This difference reflects the different propagation times of radiation from the radio source region to *Ulysses* and *Wind*. From the similarity with the event reported and analyzed by Reiner et al.

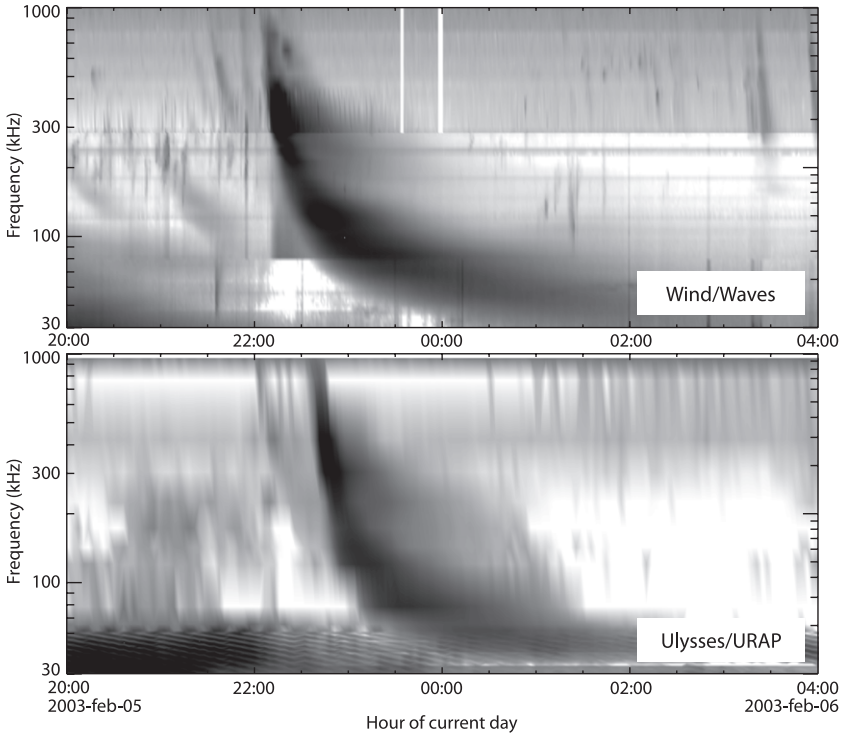

Figure 3. Dynamic spectra showing the frequency drifting type III radio bursts observed by (top) *Wind* and (bottom) *Ulysses*, covering a time interval including QPP events in X-rays on 2003 February 5 and 6.

Table 3
Characteristics of Type III Bursts Associated With QPPs on 2003 February 5 and 6

Frequency Drift	Time	Importance	Source
23–45 MHz	21:12	Low	Culg.
250–700 kHz	21:27	Low	*Wind*
200–800 kHz	21:39	Low	*Wind*
150–5400 kHz	21:55	Low	*Wind*
30–1000 kHz	22:14	Moderate	*Wind*
40–90 MHz	02:23	Low	Culg.
40–90 MHz	02:40	Low	Culg.
40–90 MHz	02:56	Low	Culg.

Note. The events are either reported by the Culgoora station (in edited solar events lists from NOAA), or observed in radio spectral data from WAVES/*Wind*.

(1998), we deduce that the radio source trajectory is expected to be typically close to the ecliptic plane and along a Parker spiral of the interplanetary magnetic field.

Several low-intensity type III bursts occur in relation to both QPP sequences. During QPP1, they occur at time intervals similar to the periodicities found in the X-ray time series. Ground-based and *Wind* events are shown in Figure 1(c) and the quasi-periodic type IIIs at *Wind* can be related to *Ulysses* events in Figure 3. However, in order to determine the time correlations with the QPP observed in X-rays, propagation delays of minutes to tens of minutes (at 1 AU or at 4.6 AU) must be added to the X-ray events. These time delays depend on the frequency ranges in which individual type III bursts are detected. During QPP2, no significant burst activity is recorded by *Wind* and very faint ∼300–940 kHz type III storm events are seen at *Ulysses* (Figure 3), while higher frequency type III bursts are recorded by ground-based observatories (Figure 1(d)).

The heliospheric longitude of source region A does not differ substantially from that of source region B. Thus, the difference observed in type III detections between QPP1 and QPP2 intervals is likely caused primarily by the difference in the range of frequencies used, in other words, the coronal heights or heliospheric distances reached by the accelerated electrons. The longitudinal angular width of directivity emission is known to increase as the frequency decreases, presumably due to propagation effects in the interplanetary medium (e.g., Bonnin et al. 2008). During QPP1, *Wind* and *Ulysses* appear therefore to be located in the wider radiation beams from the lower frequency type III bursts. However, some of the flare events associated with QPP2 produce higher frequency (40–90 MHz) type III bursts, and thus occur at lower coronal heights. This frequency range is above the instrumental range of *Wind* and *Ulysses*.

Finally, it may be noted that the type III bursts reported are quite moderate in intensity, as expected from the energies of microflares (see also Christe et al. 2008, their Figure 1). We conclude that the detection of quasi-periodic type III bursts (as reported here most convincingly in relation to QPP1 in soft X-rays) is consistent with the repeated signatures of flaring QPPs, though it naturally depends on favorable relative positions between the flare site and observer and the adequate frequency range of instruments used.

2.3.2. Microwave Emissions

QPP2 is observed in radio microwave emission at 17 GHz with the ground-based Nobeyama Radioheliograph (NoRH). High cadence images with a spatial resolution of about 5 × 5 arcsec^2 pixel^{-1} are obtained for this sequence by way of the NoRH synthesized imaging software. We retain the maximum value for any pixel in the region overlaid in Figure 2(c). The magenta solid line in Figure 1(c) shows the resulting radio time profile. The flare (2a) and the following pulsation (2b), and to

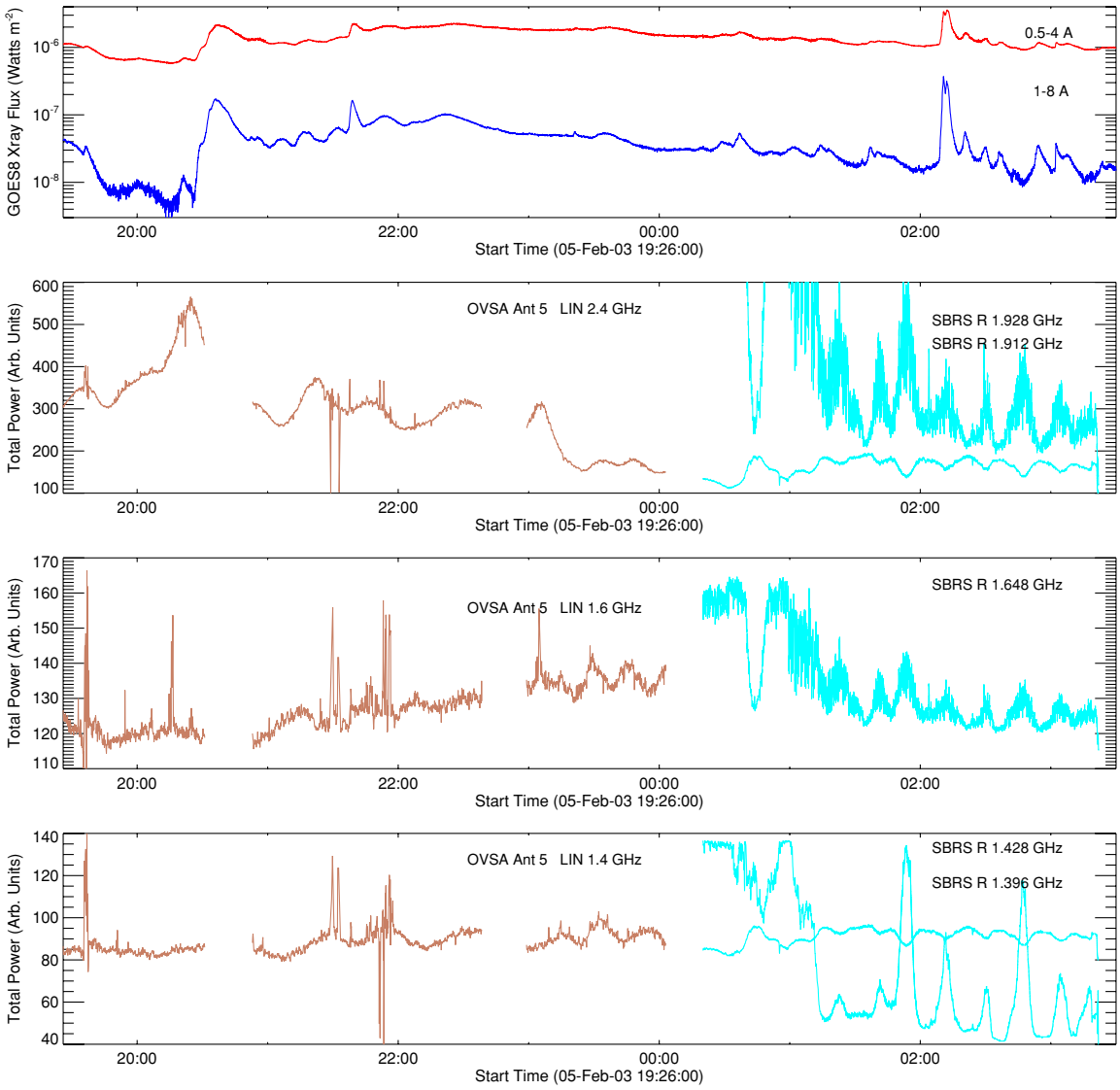

Figure 4. Top: full disk measurements in X-rays from *GOES*-8 (1–8 Å and 0.5–4 Å) and (bottom three) radio emissions (arbitrary units) at fixed frequencies near 2.4, 1.6, and 1.4 GHz, respectively, from OVSA (brown) and SBRS (cyan), covering a time interval including QPP events in X-rays on 2003 February 5 and 6.

(A color version of this figure is available in the online journal.)

a lesser extent the subsequent pulsations, show up well in the radio microwave data.

Spatially unresolved radio microwave emission at lower frequencies, between 1 and 2 GHz, is also found to display long-period oscillations during the two QPP sequences but also outside the QPP sequences observed primarily in X-rays. This finding is supported by two data sets from different instruments: the American Owens Valley Solar Array (OVSA) and the Chinese Solar Broadband Radiospectrometer (SBRS/Huairou). The OVSA points to S15 E49, i.e., toward AR10276, 8° longitude west and 7° latitude north of source region A (AR10277) and is operating in time intervals overlapping with QPP1, while the SBRS is operating in a time interval including QPP2. In the 1–2 GHz range, the SBRS has a frequency resolution of 4 MHz, while the OVSA has a resolution of 200 MHz. Figure 4(b) shows a few examples of radio emission (arbitrary units), at 1.396, 1.428, 1.648, 1.912, and 1.928 GHz from SBRS (right polarization) and at 1.4, 1.6, and 2.4 GHz from OVSA using Antenna 5 (linear polarization). Although the data sets do not overlap in time, they show that emission at similar radio frequencies display oscillations with similar periods. The long periods (∼18 minutes) observed in the OVSA and SBRS radio data are about twice those of the X-ray QPPs. Further analysis of the SBRS data is presented and discussed in Section 4.

2.4. X-ray Observations

RHESSI images in the energy range 5–12 keV showed two closely spaced and compact sources or "kernels" in each flaring site, originating from the top or apex of the small loops in agreement with available Extreme-UV images (F05, their Figure 3 panels (a) and (d)) and therefore interpreted as double coronal sources. We examine this feature in greater detail in Figure 5, with *RHESSI* images formed using the CLEAN algorithm (Hurford et al. 2002) and uniform weighting over 62 s integration (15 collimator rotations).

The particular case detailed here shows, for both QPP sequences, the recurring appearance of a second coronal source. The separation between the two sources is of the order of 10 arcsec. One loop-top source in X-rays is standard (e.g.,

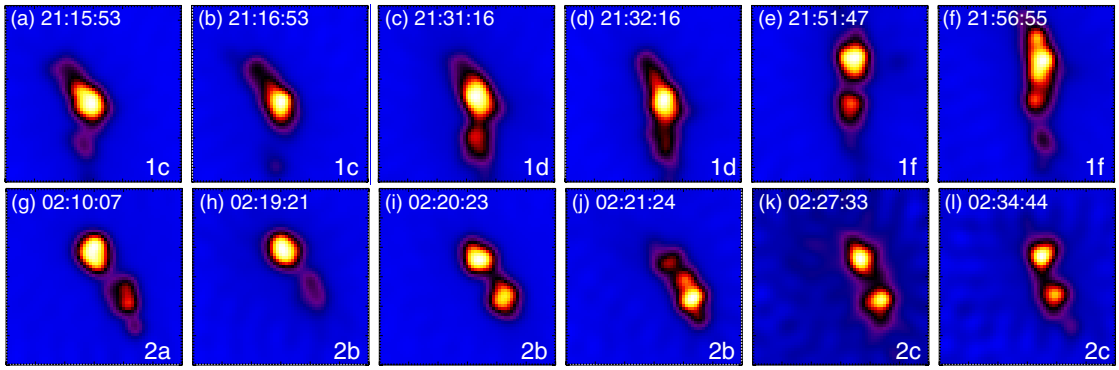

Figure 5. *RHESSI* images representative of three individual flarings in each QPP sequence for (top row) QPP1 on 2003 February 5 and (bottom row) QPP2 on 2003 February 6, shown in the 5–12 keV energy range. The individual flaring event is identified in the lower right-hand corner of an image. The images are reconstructed from collimators 1F and 3F–6F at the start time indicated in each image and for a duration of about 62 s. The FOV for each image is centered on heliocentric coordinates (top row: region B, northern hemisphere) $X = -856 \pm 20$ and $Y = 380 \pm 20$ arcsec and (bottom row: region A, southern hemisphere) $X = -770 \pm 20$ and $Y = -222 \pm 20$ arcsec.

(A color version of this figure is available in the online journal.)

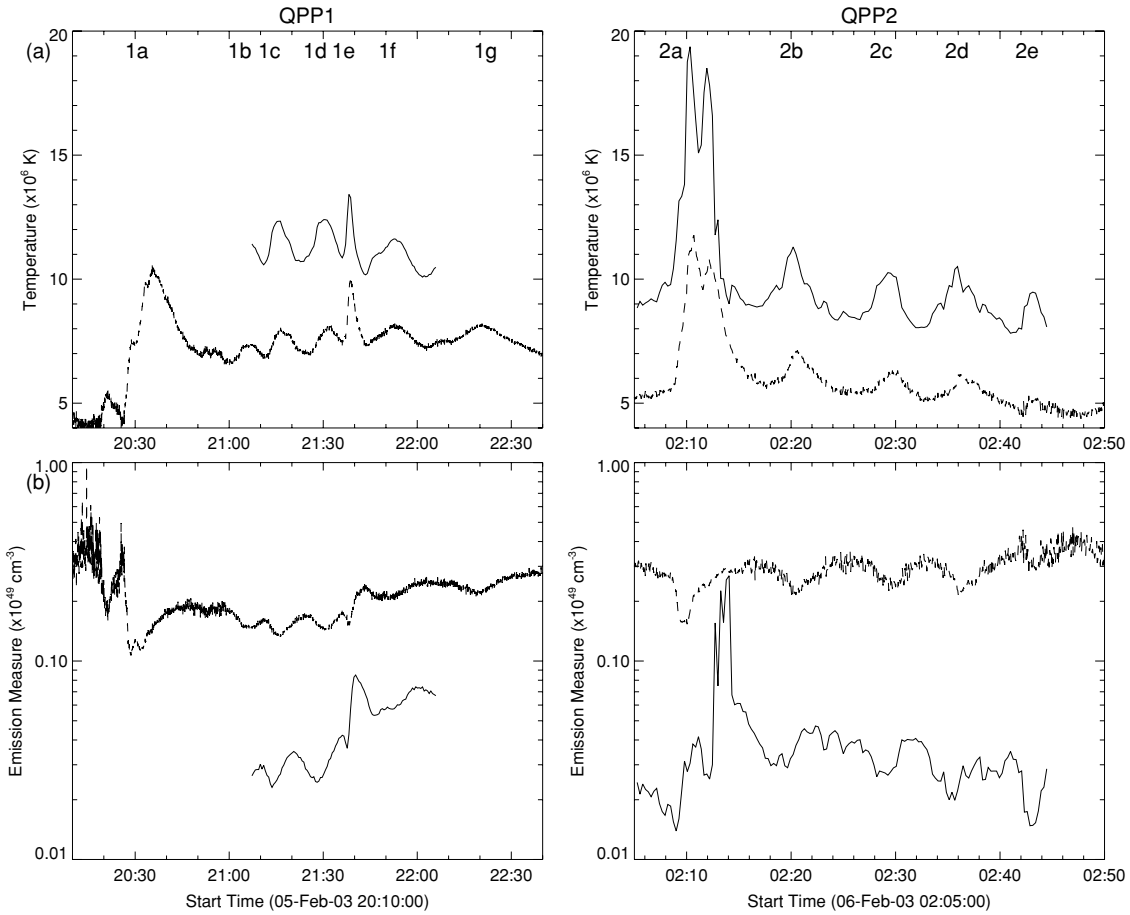

Figure 6. Temperature and emission measures for the QPPs on 2003 February 5 and 6, as derived from *RHESSI* spectral analysis (thick solid lines) and using the two *GOES* channels (dashed lines).

Kahler 1977; Acton et al. 1992; Sui et al. 2005). However, more and more evidence for the appearance of a double X-ray source in the 5–25 keV energy range has been reported (Sui & Holman 2003; Sui et al. 2004; Veronig et al. 2006; Milligan et al. 2010). In QPP1, the event (1e), not shown, originates from a neighboring loop slightly to the southeast of the pulsating coronal source(s). Panels (h)–(j) show the transition on a 2 minute timescale from one dominant kernel to the other. In this particular sequence, the first upper source may be seen either to dim, relative to the second lower source, or to move toward and merge with the second source. This occurs at the precise time of the pulsation peak (2b), at 02:20:30 UT (see Table 2). The positions of the kernel(s) and the separation between the two kernels at each pulsation peak may vary during each QPP sequence. However, position fluctuations on such small scales are consistent with noise at the instrumental level.

In Figure 6, temperatures and emission measures during the QPPs are derived either from *RHESSI* spectral analysis or using the two *GOES* channels. *RHESSI* thermal fits are obtained with a spectral function that includes an isothermal part based on the

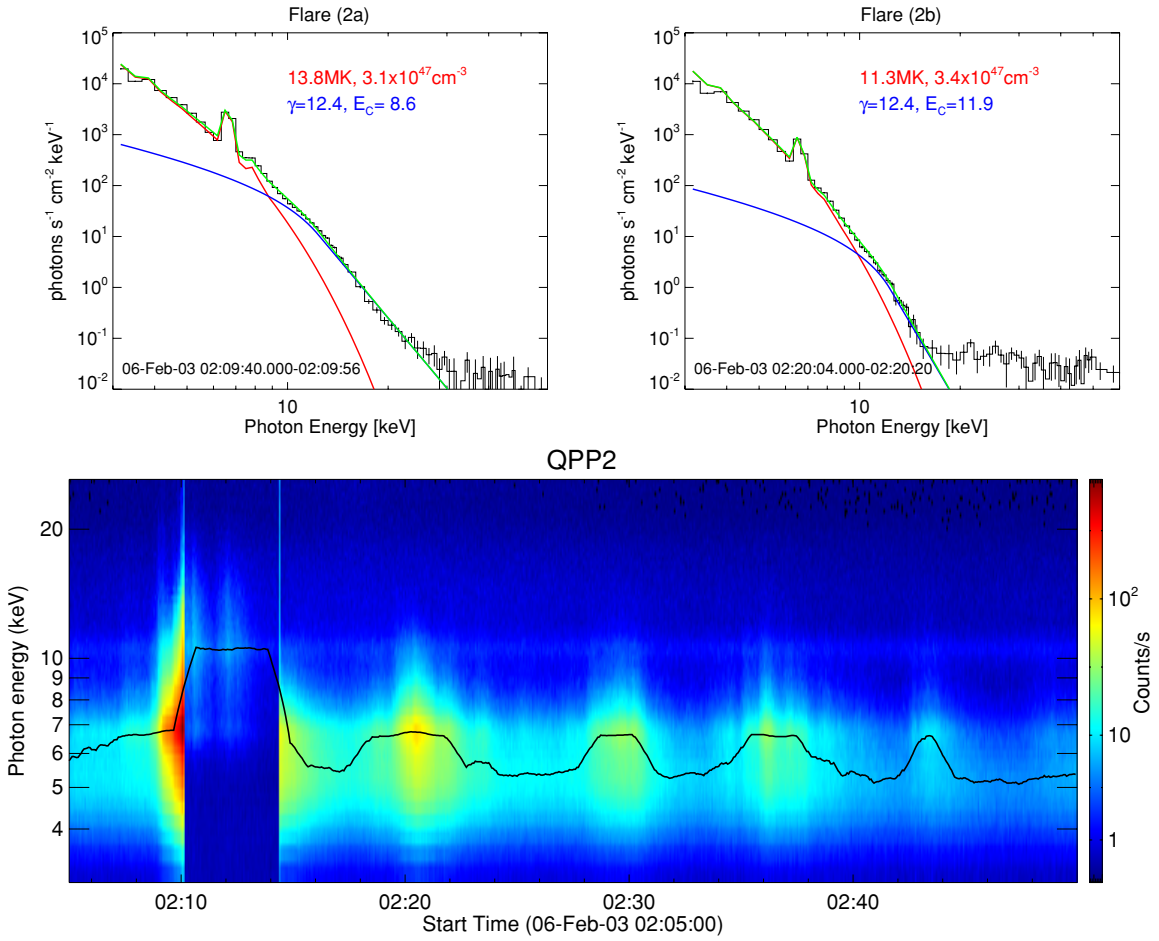

Figure 7. *RHESSI* spectral data for QPP2 on 2003 February 6. Top: photon spectra (vs energy) during flare events (2a) and (2b), with overplotted spectral fit (green) combining thermal (red) and non-thermal (blue) components; the indicated fitted parameters are the thermal temperature, emission measure, non-thermal power-law γ exponent, and energy cutoff E_c. Bottom: spectrogram of count rates (vs. photon energy over time): for most of the time range, *RHESSI* was in A0 (zero attenuation) state, with a short ∼4 minute interval during flare (2a) in A1 (thin attenuator) state when the count rate was reduced; the solid black line shows the energy of maximum photon counts.

(A color version of this figure is available in the online journal.)

CHIANTI atomic code with coronal abundances (e.g., Phillips 2004), plus a nonthermal contribution which is a thick-target approximation with a power-law energy distribution of electrons (Holman 2003). Examples of such fits are presented in the top panels of Figure 7. The *GOES* parameters are derived from the ratio of the intensities of the two *GOES* soft X-ray channels using an expression given by White et al. (2005), which assumes an isothermal plasma and coronal (CHIANTI) abundances. There is a difference in the temperatures, with those from *GOES* on average 3–5 MK less than those from *RHESSI* (for the flare peak (2a) the difference is up to 8 MK), illustrating the non-isothermal nature of the plasma.

The flare (2a) in QPP2 was studied by Sylwester et al. (2008) using high-resolution soft X-ray spectral observations with the RESIK instrument (covering the period 02:08–02:32 UT). The He-like argon (Ar XVII) line emission at ∼3.9 Å, analyzed by Sylwester et al. (2008), is excited by energies (∼4 keV) comparable to those of the two *GOES* channels, and so the temperatures deduced from the Ar XVII line ratios are similar to those from *GOES*. This is confirmed for the so-called *G* line ratio, defined by Sylwester et al. (2008) and measured every ∼17 s during the 02:09–02:15 UT interval, which tracks the temperature from *GOES*. However, two measured values of *G* are anomalous, each at the start of the peaks denoted by (2a), giving rise to the possibility of non-thermal excitation of some of the Ar XVII lines. The *RHESSI* photon spectrum in the upper left panel of Figure 7 shows a significant non-thermal component (blue fit) during the impulsive part of this flare. The spectral fit to flare (2b) (upper right panel) illustrates that the non-thermal component is also present in subsequent flares, albeit weaker.

Within the multi-thermal plasma, we obtain large oscillations in temperatures (around 5–8 MK for *GOES* and 10–12 MK for *RHESSI*), with the same 10 minute periodicity as in the light curves. Emission measures oscillate in phase opposition with the temperatures. Although this property is seen with two separate instruments, it could result from artifacts due to the functional form of the fitted isothermal model (combined with a poorly known instrumental response of *RHESSI* at low energies). Nevertheless, the oscillations show significant phase differences between the *RHESSI* and the *GOES* parameters, with variations at higher temperatures (from *RHESSI*) leading the ones at lower temperatures (from *GOES*). From the parameters derived with the *RHESSI* spectral analysis (to a lesser extent with *GOES*), it can also be noted that while the rate of change in background intensity levels (positive in QPP1 and negative in QPP2) correlates with the overall background changes in emission measures, the temperature background level decreases in both cases. The oscillations can be further illustrated with

the lower panel of Figure 7, showing a *RHESSI* spectrogram of count rates (displayed versus photon energy over time) for QPP2, where the energy width of the count spectrum (at a given level of count rate) is smaller for inter-flare periods than for the flare events. The energy location of maximum counts is in the 5–12 keV range due to the convolution of the falling photon spectrum and the instrumental absorption, particularly at low energies (below 5 keV). As a result, for the period when *RHESSI* was in its A0 (zero attenuation) state, the energy of maximum photon counts peaks at the 6.7 keV Fe line in flarings (2b–d) and decreases in the inter-flare periods.

3. COMPARATIVE ANALYSIS ACROSS THE ENERGY SPECTRUM

In order to compare the different energy curves displaying the oscillations in QPP2, a few transformations are performed. The radio brightness NoRH temperature averaged in region A is smoothed with a 10 s boxcar running average, yielding the radio time series of type $I(t)$. For the full-disk soft X-ray time series, it is useful to define the time series as $J(t) = \sqrt{I(t)}$, assuming thermal emission of the form $I \sim n_e^2$; the series are interpolated to a regular 1 s cadence time array. The wavelet "à trous" transform (Starck & Murtagh 2002) is used to obtain the trend (I_o or J_o) of each time series (see also F05); see left panels of Figure 8. The trend corresponds to the background flare temperature or density, which decreases noticeably during the QPP2 sequence. To account for these changes and for meaningful comparison between variation amplitudes across the energy spectrum, we use the de-trended time series (i.e., $I/I_o - 1$ for the radio data and $J/J_o - 1$ for the others).

In a first instance, a cross-correlation analysis is performed on the de-trended time series. The analysis shows that the time series are best correlated for time delays between some of them. See Table 4. The time series for the *RHESSI* energy bands (3–6 keV, 6–12 keV, and 12–25 keV) are coincident to within 1 s. Going from higher to lower energies, the *GOES* time series lag the *RHESSI* time series by 7 s and 15 s. The radio time series lags all the other time series, by up to 20 s with respect to the *RHESSI* time series.

In a second instance, the de-trended time series are each fitted with a cosine curve $F(t)$ with a linear period change and exponential decay, viz,

$$F(t) = A \cos\left(\frac{2\pi t}{P_o + \lambda t} - \phi\right) \exp\left(-\frac{t}{\tau_d}\right), \qquad (1)$$

for amplitude A, initial period P_o, linear period change rate λ, phase ϕ, and damping time τ_d. Using a nonlinear least-squares fit algorithm and with all parameters kept free, an initial fitting of each curve yields poor estimates of λ for the radio and the *RHESSI* 12–25 keV time series (with non-zero minimum convergence tolerance of the computation), and much better and consistent estimates for the other time series. With zero tolerance, the fit to the *RHESSI* 6–12 keV curve gives the best estimate $\lambda = -0.051 \pm 0.004$ s^{-1}, i.e., a slight decrease in P from $P_o = 10$ minutes to 8 minutes during the duration ($\Delta t = 40$ minutes) of the oscillations. Choosing λ to remain fixed to this value, a second fitting of the time series is performed, where all the computations were successful with zero tolerance. The results are those shown in the right panels of Figure 8 and presented in Table 4.

We find a good agreement between the time series for an initial period $P_o = 10$ minutes. The oscillations in the 12–25 keV

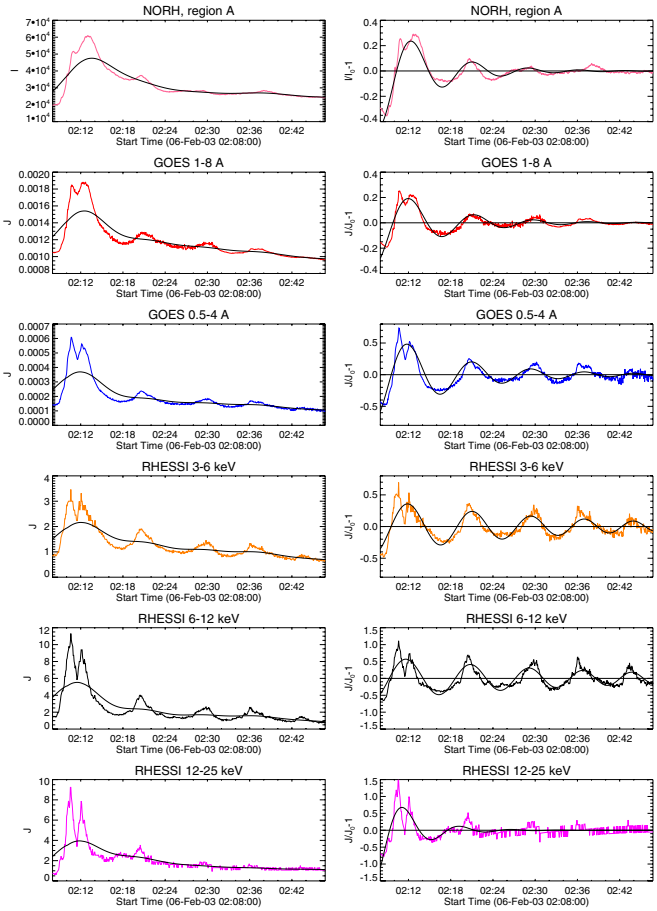

Figure 8. Left: NoRH time series I of the average temperature brightness in region A, and the *GOES* and *RHESSI* time series $J = \sqrt{I}$, with trends (I_o or J_o) overlaid as thick solid lines. Right: corresponding de-trended time series $I/I_o - 1$ and $J/J_o - 1$ and overlaid fits (thick solid lines).
(A color version of this figure is available in the online journal.)

RHESSI curve are too weak and particle emission between flarings (2a) and (2b) interferes with the fit accuracy. The results for this energy band are therefore less representative. The assumption of identical period change throughout the energy range therefore appears justified and is also supported by the in-phase energization of particles in the energy spectrum around 6 keV (lower panel of Figure 7). However, there are phase differences between spectral energies, consistent with the time delays obtained from the correlation analysis; see Figure 9(a). The damping times increase with growing energy up to $\tau_d \approx 2.84\, P_o$ for the 6–12 keV energy curve (see panels (b) and (c) of Figure 9).

4. CORONAL OSCILLATIONS IN 1–2 GHz RADIO SPECTRA

Panels (a)–(c) of Figure 10 present a section (1.36–1.48 GHz) of 1–2 GHz radio dynamical spectra from SBRS, encompassing the QPP2 interval. In a given circular polarization mode, left (L) or right (R) circular polarization (panel (a) or (b)), the radio spectrum reveals that the long-period oscillations seen at fixed frequency correspond to decimetric pulsating structures (DPSs), with no drift in frequency. The absolute degree of polarization associated with the DPS is above 10% (see panel (c)), which indicates reliable instrumental observations (Fu et al. 2004). Those types of narrowband continuum DPS have been observed

Table 4
Results of Cross-correlation and Curve Fitting Across the Energy Spectrum for QPP2

Data Type X	X	Y	$P_{XY}(L)$	L (s)	A	ϕ (rad)	P_o (minutes)	τ_d (minutes)	τ_d/P_o	σ
Radio 17 GHz	1	2	0.908711	−5	0.44 ± 0.14	3.11 ± 0.34	9.55 ± 0.81	7.21 ± 3.10	0.75	0.0367
X-rays 1–8 Å	2	3	0.955372	−8	0.31 ± 0.15	2.69 ± 0.37	10.14 ± 0.93	8.41 ± 5.13	0.83	0.0272
X-rays 0.5–4 Å	3	4	0.910569	−7	0.70 ± 0.06	2.55 ± 0.08	10.03 ± 0.16	10.55 ± 1.32	1.05	0.0815
X-rays 3–6 keV	4	5	0.959686	0	0.42 ± 0.09	2.54 ± 0.17	10.01 ± 0.16	22.71 ± 8.08	2.27	0.0930
X-rays 6–12 keV	5	6	0.800975	−1	0.65 ± 0.04	2.37 ± 0.06	10.00 ± 0.05	28.36 ± 3.24	2.84	0.1613
X-rays 12–25 keV	6	...	...	...	1.37 ± 0.23	2.52 ± 0.12	8.77 ± 0.43	4.62 ± 0.92	0.53	0.1641

Notes. Maximum cross-correlation coefficient P_{XY} of de-trended time series X and Y for lag L. Amplitudes A, phase ϕ, initial periods P_o, and damping times τ_d of oscillations obtained by curve fitting of time series X to Equation (1) with fixed period change rate $\lambda = -0.051$ s^{-1}; σ is the weighted standard error of estimate (i.e., the average scatter of the points from the fitted curve).

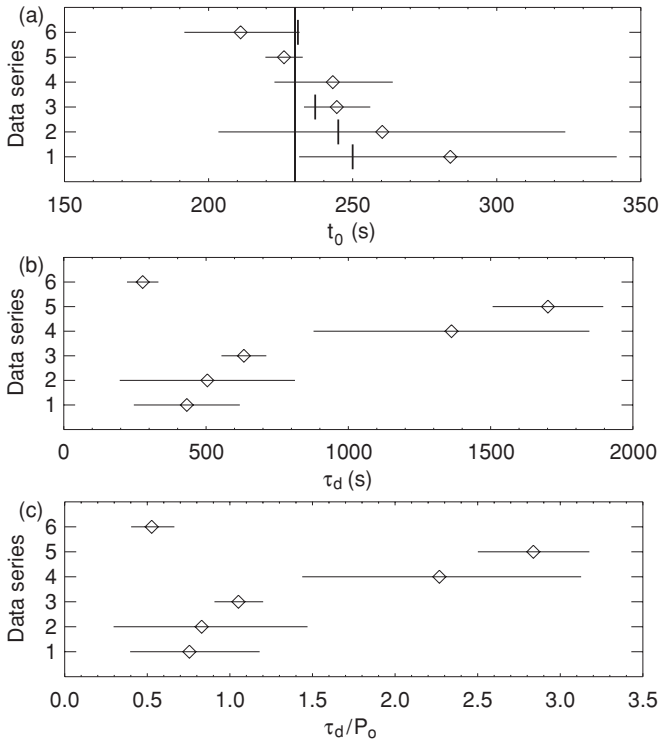

Figure 9. Comparative analysis of QPP2 for spectral energies numbered from 1 to 6 in Table 4, i.e., increasing in temperatures in the soft X-rays, illustrating curve-fitting results marked with diamonds and within horizontal error bars. (a) The phase differences represented by the times $t_o = \phi P_o/(2\pi)$ are consistent with the time delays obtained from cross-correlation analysis, represented with short vertical lines, with respect to a reference time chosen at 230 s (first long vertical line); (b) damping times τ_d, and (c) ratios τ_d/P_o increase with spectral energies up to 6–12 keV.

before (e.g., Karlický 2004; Kołomański & Karlický 2007), but not with such quasi-periodic behavior.

In addition, the current observations reveal a pattern of three narrowband continuum DPS (the bandwidth is about 16–20 MHz), with the middle band emission much weaker and in opposite phase to the emission from the other two surrounding bands. The lower panel of Figure 4 shows the emissions at 1.396 GHz and 1.428 GHz in the *R*-mode, which correspond to the upper and middle bands of Figure 10(b). The pattern repeats itself at least four times between 1 and 2 GHz, every 232 or 252 MHz. For instance, the 1.164, 1.208, and 1.276 GHz bands form such a group in the *R*-mode (not shown). The two center panels of Figure 4 show a selection of DPS bands from the other groups in the *R*-mode. Although the time cadence is high (0.2 s), the time lags between the time series from separate frequency bands cannot be reliably found because of the high noise level.

The polarized and narrowband emission between 1–2 GHz indicate non-thermal (gyroresonance) emission from high energy electrons rather than thermal (bremsstrahlung) emission from hot plasmas. We rule out non-thermal gyrosynchrotron emission, which typically dominates above 3 GHz. In the case of gyroresonance emission, *R* and *L* polarizations indicate angles between the magnetic field direction and the line of sight (LOS), which are less or greater than 90°, respectively (White 2004). Right and left polarized oscillatory signals may alternate, without being completely out of synchronization. This is shown in panel (d) at the frequency of 1.396 GHz, with the corresponding signed polarization in panel (e). The corresponding narrowband continuum DPSs in the *R*- and *L*-modes (with opposite maximum emissions) are close (the *L* bands may have frequencies 4 MHz higher than the *R* bands).

Following previous interpretations of DPS, we first assume the radio DPS emission to be directly related to the ambient conditions in the vicinity of a moving plasmoid. Since we do not detect CMEs prior to QPP2, the lack of frequency drift is consistent with the absence of plasmoid ejection. Moreover, since the radio data indicate patterns of DPS, which alternate in emission between left and right polarizations, we deduce that the narrowband continuum DPS can result from a moving plasmoid, which has a transverse oscillatory motion with respect to the LOS (see sketch in Figure 11). The plasmoid may correspond to the cross section of a large-scale magnetic loop, oscillating with an ∼18 minute period. The repetitive patterns of narrowband continuum DPS, which are not damped, can therefore be attributed to plasmoid/loop oscillations in the background corona (in this case, the plasmoid structure, traditionally invoked in association with radio DPS emission, is likely to have a helical flux rope topology). The transverse motions to the LOS necessary to explain the polarization signatures point to a (fast) kink mode of oscillation. Other MHD modes can be ruled out for the following reasons. If the observed 18 minute period modulations were caused by the fast sausage mode, then the loop structure supporting non-leaky oscillations would need to be unrealistically wide and/or dense for a large quiescent loop (see Nakariakov et al. 2003). As for the (slow) compressional mode, it would be relevant if it could modulate gyrosynchrotron emission via the Razin suppression (Nakariakov & Melnikov 2006), but gyrosynchrotron emission is not the mechanism identified here.

The multi-structured emission could be caused by multiple loops. A rough approximation to the length of the oscillating loop(s) may be deduced via MHD coronal seismology. In a long wavelength and cold plasma approximation, the period of

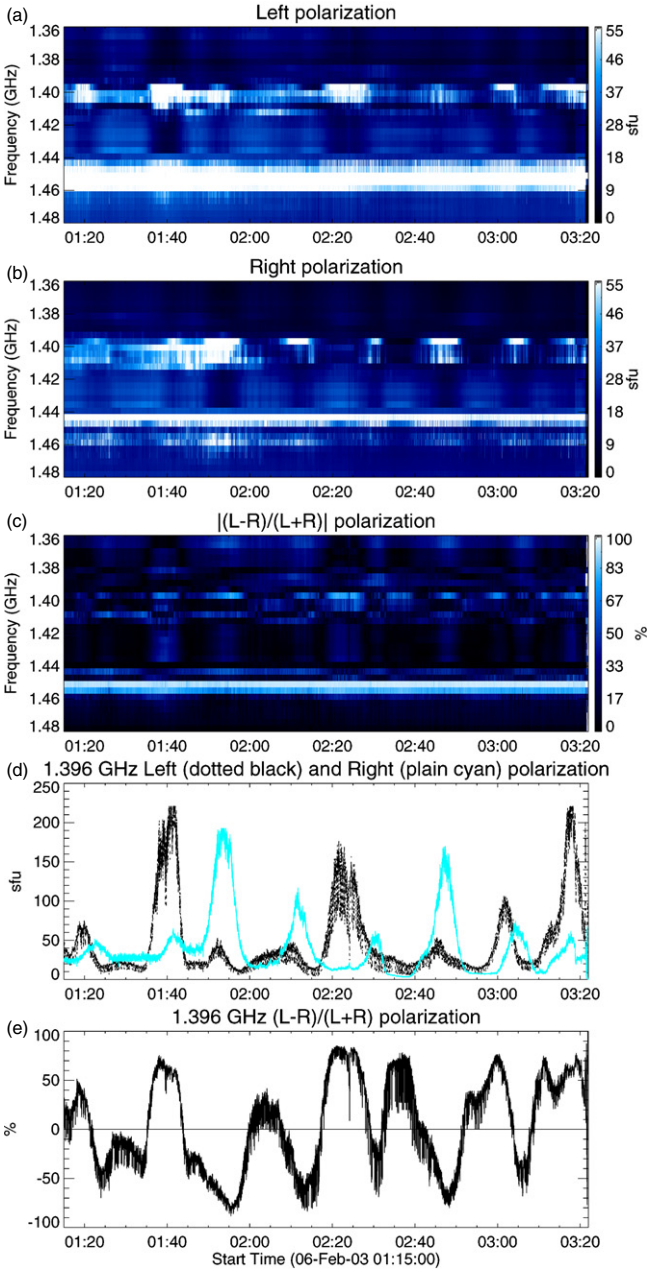

Figure 10. (a) Left polarized, (b) right polarized, and (c) absolute polarization of SBRS radio dynamical spectra on 2003 February 6, showing decimetric pulsation structures (DPS) forming one pattern (in the 1.36–1.48 GHz frequency range) of three narrowband continuum (with bandwidth of 16–20 MHz). The white horizontal line in panel (a) is caused by strong interference. A minimum background is subtracted from the time series at each frequency. A polarization above 10% indicates reliable instrumental observation of the DPS. Left and right polarized oscillatory signals may alternate, without being completely out of synchronization. This is shown in panel (d) at the frequency of 1.396 GHz, with the corresponding signed polarization in panel (e), which indicates the direction of the magnetic field with respect to the LOS.

(A color version of this figure is available in the online journal.)

the fast magnetoacoustic kink fundamental mode is (Edwin & Roberts 1983)

$$P \sim \frac{2L}{C_k} \sim \frac{\sqrt{2(\rho_0 + \rho_e)\mu_0}}{B_0} L \qquad (2)$$

for a loop of length L modeled as a straight cylinder, with internal magnetic field B_0 and density ρ_0 and external density ρ_e; C_k is the kink speed and μ_0 is the magnetic permeability.

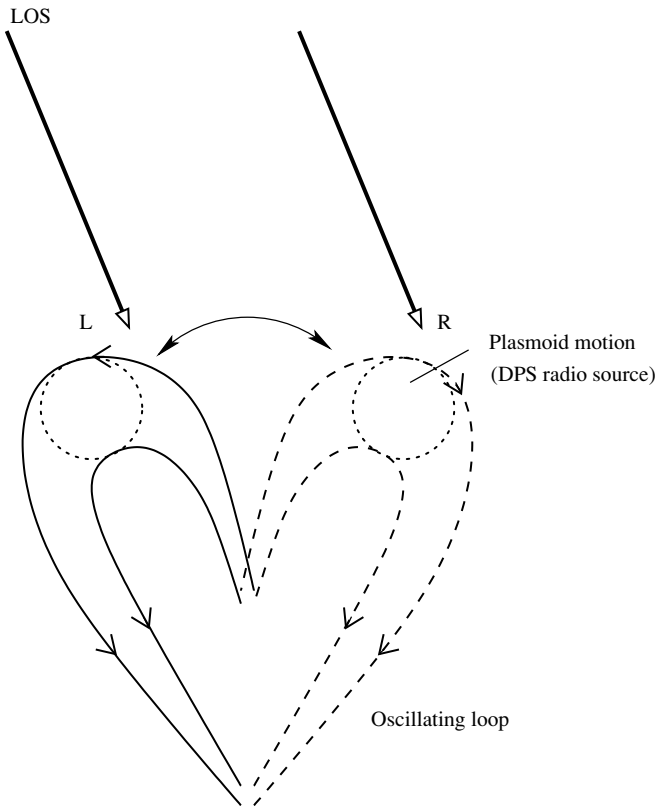

Figure 11. Sketch of the mechanism for the generation of quasi-periodic narrowband continuum of decimetric radio emission (DPS). A moving plasmoid corresponds to the cross-section of a loop experiencing transverse fast magnetoacoustic oscillations with respect to the line of sight (LOS), i.e., a kink mode. The transverse motion explains the patterns of DPS, which alternate in emission between left (L) and right (R) polarization, with the period of the oscillating loop.

Employing this approximate expression and assuming the values $B_0 = 10 \pm 5$ G and $\rho_e = 10^8$ cm^{-3} in the ambient upper corona and a density contrast between external and internal loop environments, $\rho_e/\rho_o = 0.1$, we obtain an estimate of the loop length to be 1,410 $\pm$ 705 Mm, which is larger than the estimated length of the TEL connecting regions A and B (F05). This interpretation is qualitatively plausible as the 18 minute periods are detected by OVSA, on February 5, above another region on the disk, near region A (Section 2.3.2).

5. DISCUSSION

5.1. Nature of Flaring Events

There are clearly fast non-thermal electrons present in the event. In the transition region, they produce bremsstrahlung emission and heating there. In the corona, they produce type III radio emission (relativistic electrons in the corona). In the chromosphere, they produce the Hα signature, which is usually associated with the response of the chromosphere to bombardment by electrons or strong thermal conduction.

The phase differences between the plasma parameters of high and low temperatures (Section 2.4) or between the emission light curves of high and low energies (Section 3) suggest a thermalization of the most energetic electrons heating the soft X-ray-emitting plasma at lower energies. From the likely thermalization in the loop and the absence, in *RHESSI* imaging, of hard X-ray emission co-spatial with even the strongest Hα ribbons, we deduce that the observed chromospheric response

is due to thermal conduction. Correlated observations of the low-energy X-ray emission with the radio microwave emission at 17 GHz, available in one instance (QPP2), are consistent with a thermal interpretation. In the absence of significant hard X-rays, chromospheric evaporation is thus believed to be mainly produced by heat conduction fronts. The magnetic reconnection process in a coronal X-point is thought to accelerate particles as well as to heat up the local plasma. The subsequent evaporated plasma may contribute to increase the densities and therefore the emission measures observed between the flarings. Although, in this event, the instrumental limitations prevent such evidence for chromospheric evaporation to be reliably admitted, it is an expected response to chromospheric energy input as observed in the Hα emission.

5.2. Mechanisms for Long-period QPPs

It is reasonable to assume that the basic mechanisms in the two flaring sites are the same. F05 argued, from the available observations, that the flare-induced long-period QPP could be explained as modifications of the emission in the small flaring loops due to the fast kink MHD waves in a magnetically linked and large-scale loop. From the present extended observational analysis, we seek to identify how this configuration favors reconnection in the flaring sites, giving rise to repeated episodes of reconnection between the two structures as the larger one oscillates. Several mechanisms may be envisaged based on the interaction between the total pressure perturbation, caused by the fast wave evanescent tail outside the resonating loop and a pre-existing current sheet above the small-scale loop; this interaction occurs at a particular phase of the oscillation, due to the transverse displacement of the resonating loop. For instance, the pressure perturbation may be sufficiently large to thin the current sheet and trigger reconnection. Alternatively, it may induce periodic variations of electric current density in the current sheet, leading to current-driven plasma micro-instabilities and enhanced resistivity (Nakariakov et al. 2006). The proposed scenario gives rise to one coronal (loop-top soft X-ray) source at a time.

To explain the second coronal source, which is seen to occur in the *RHESSI* images for a relatively cool (temperature $T = 10$ MK) plasma and for small-scale sizes of the flaring loops, we need to consider additional scenarios. For instance, reconnection itself may result from a periodically triggered resistive instability, either (1) a tearing mode and/or (2) a thermal instability. The tearing mode, indicating the existence of one or more plasmoids, is suggested by the presence of more than one coronal source (e.g., Sui et al. 2005). Alternatively, the localized cooling of coronal plasma by the thermal instability implies a rise of classical electrical resistivity ($\eta \propto T^{-3/2}$), which may help to induce magnetic reconnection (Kliem et al. 2002). Temperature variations in the reconnection configuration could therefore modulate the reconnection rate. We suppose that those temperature variations result from a radiative instability in the plasma (due to shorter radiative timescales in the sources of interest), as a result of periodically changing plasma density in the small flaring loop due to chromospheric evaporation (radiative loss rate is $\propto n_e^2$). As chromospheric evaporation may occur on similar radiative cooling timescales as the QPP periods, the thermal instability could presumably give rise to one of the coronal X-ray sources.

Those instabilities are not necessarily exclusive, but we conclude that, for the generation of long-period QPPs, they both appear as secondary processes that could enhance the driving mechanism of fast kink MHD waves in a magnetically linked and large-scale loop. The most efficient triggering of the reconnection by an external kink wave corresponds to a form of "resonance" between the kink mode of the large-scale loop and those secondary processes. In other words, preferential "coupling" or "interaction" can exist for large-scale and small-scale loops, which can mutually enhance the resistivity generated by each driving mechanism.

5.3. Period Change as a Spatial Effect

As reported in F05, there are slight but detectable changes of period in QPP1 and QPP2, characterized by period increase and decrease, respectively. Within the QPP2 sequence, the periodic flaring activity is sympathetic but asymmetric, switching progressively from region A to region B, while the harmony of the pulsating sequence is preserved. This indicates that, while the oscillation in the large resonating loop persists throughout, flaring can switch on or off in each region as local conditions change. More precisely, this form of sympathetic activity results from different preferential conditions in each site, which are met as the period changes.

What causes the slight period change itself may be linked with an evolution of the density or magnetic field strength in the resonating loop or changes in the oscillating loop length. We can exclude the effects of changes in the flaring sites on the plasma conditions in the resonating loop. Since the phase speed of fast magnetoacoustic kink wave mode tends toward the kink speed, inversely proportional to the square root of the density (see Equation (2)), we would expect that an increase in density, due to evaporation from the adjacent flaring site, would lead to a decrease in the period for a given loop length. However, the derived emission measures from *RHESSI* spectral analysis (Section 2.4) indicate the opposite (i.e., an increase/decrease in density for QPP1/QPP2). Thus, we conclude that the background density levels in the flaring sites do not greatly influence the plasma conditions in the resonating loop.

Instead, the period variations could be related to changes in the geometry of the oscillating loop, first increasing following a CME eruption at the time of QPP1, and then shrinking again, but oscillating throughout. In the event studied, QPP1 is accompanied by a small filament eruption and a corresponding CME in the same region B, while QPP2 is followed by one in the same region A. It is possible to envisage the rise of arcade field lines forming the transequatorial coronal loop (TEL), following the filament eruption at one end (region B) and the associated CME, and the TEL shrinkage prior to the next eruption, despite the ongoing flaring at one end (region A). This follows from standard post-flare behavior in a TEL, which was seen to rise with time (Švestka et al. 1995), and from evidence of a large intensity increase in TEL behaving as a flare-loop system (Khan & Hudson 2000; Harra et al. 2003).

5.4. Role of Flare Triggering on QPP Damping

As discussed in F05, the weak damping of QPPs is consistent with the damping of the kink oscillations discovered with *TRACE*, but the real decay time in the resonating loop could be much larger. In fact, there is no measurable decay in QPP1. Here we also bring evidence of $\sim$18 minute periodicities, which may be attributed to "quiet" large-scale loops (in the background corona) subject to fast kink modes of oscillation, which are not damped throughout the QPP sequences (Section 4).

It is essential to keep in mind the separation between, on the one hand, the oscillation (presumably from the external

driver) that triggers the energy release and, on the other hand, the "triggering" process itself. By triggering, we mean the early onset of the instability that causes a flare. How the plasma responds to the energization that follows over the QPP sequence is characterized by the damping. However, the intensity of the event, e.g., at its peak, is also determined by contributions of the ambient flaring plasma. In particular, the original time series in QPP2 show a background decreasing with time, so that a fit to the original data, without normalization, would yield an apparently small decay factor (larger damping). Given the long periods of the QPPs, the particles making the higher energy X-ray emission in the corona can be injected freshly at each pulse and collisionally lost very rapidly. The non-thermal X-ray emission, present around 12 keV, is always proportional to the product of injected and ambient particles, so that de-trending or normalization is necessary to remove or at least moderate the background contribution, i.e., the de-trended pulses reflect the instantaneous non-thermal electron density.

In addition, one can envisage a threshold at the flaring site, e.g., in the accumulation of anomalous resistivity, which enables the interaction between the external resonator and the flaring loop to be quasi-independent of the damping in the external resonator, if present. Once this threshold is reached, a flare event is triggered. Besides, the comparative analysis in Section 3 indicates that the decay factor τ_d/P in QPP2 is not constant, but rather increases with spectral energies (i.e., temperature in the soft X-ray) until it reaches a maximum in the 6–12 keV energy range and then decreases in the energy range above. There is thus a preferential temperature or energy range at which the QPP triggering efficiency is more amplified. Because of this amplification, the QPPs in the 6–12 keV energy range also yield the best initial curve fit and the best estimate for period change rate.

Finally, while we note that the global appearance of damping is preserved in QPP2 despite the sympathetic activity (progressively switching from one region to another), sympathetic activity itself can be an important factor leading to QPP damping. We conclude that there is no evidence of damping per se of the kink mode in the external resonator and that the effect of damping appears to result from the triggering process itself. In other words, the flaring oscillation amplitudes decrease with time because of evolving conditions in the flaring sites, rather than a presumed damping in the resonating loop.

6. CONCLUSION

The extended analysis of the long-period QPP events of 2003 February 5 and 6, first reported by F05, provides a comprehensive picture that is consistent with a dense flaring loop subject to periodic energization and thermalization. The energization explains the occurrence of moving streams of electromagnetic radiation in the heliosphere (type III bursts). Our key results can be summarized as follows.

1. We observe QPPs in Hα and interplanetary radio type III bursts, with similar periods ($\sim$10 minutes) as the QPPs in soft X-rays. Such periods are the longest ever reported for those types of data sets.
2. We produce and detail images of double coronal soft X-ray sources, for the first time associated with long-period QPPs, which could be the particular signatures of a magnetically linked large-scale loop, acting as the main driving mechanism for the QPPs. Sympathetic activity between the two sites connected by the large-scale loop may result from different preferential conditions in each site, which are met as the period changes. Changes in the oscillating loop length are the likely cause for the QPP period changes.
3. We report a 1–2 GHz radio emission, multi-structured at regularly separated narrowband frequencies and modulated with $\sim$18 minute periods, consistent with multiple "quiet" large-scale outer loops, possibly under a streamer current sheet. Large-scale but shorter inner loops below may act as preferential resonators, with $\sim$10 minute periods. The observations support interpretations consistent with both inner and outer loops subject to fast kink MHD waves. Arguably, the period ratio of $\sim$2 could be interpreted as a signature of parametric resonance.
4. There is no evidence of damping of the kink mode in those loops, while the damping of QPPs appears to arise from the triggering process, which is more efficient in a specific temperature or energy range and is affected by evolving conditions in the flaring sites.
5. The region where the inner loops could be magnetically-coupled to a given flaring site is identified as one of two coronal sources in X-rays. The second coronal source may result from tearing or thermal instabilities. The thermal instability process (Kliem et al. 2002), combined with radiative cooling dynamics, could also explain in general long-period QPPs in single active regions on the disk. Moreover, since hard X-ray flares (flares with a higher hard X-ray flux) also have higher temperatures (e.g., Battaglia et al. 2005), where conductive cooling may dominate and occur rapidly (with a faster rate than radiative cooling), this would explain why the long-period QPPs are less likely to be present in the hard X-ray flares.

Thus, long-period QPPs in solar flares may result from a fine balance between scale sizes and dominant energetic processes. This preferential coupling is a form of resonance, which may give rise to the long-period QPPs observed in solar flares only when certain conditions are fulfilled. The discussed mechanisms are of particular relevance to the interpretation of sympathetic flaring and similar phenomena in stellar flares.

C.F. acknowledges financial support from the UK Science and Technology Facilities Council (STFC) on the CFSA Rolling Grant and a Royal Society International Travel Grant for her visit to China. L.F. and I.G.H. acknowledge the support of Rolling Grant ST/F002637/1 from STFC, and the EU's SOLAIRE Research and Training Network (MTRN-CT-2006-035484). Special thanks to Y. Yan and the SBRS team and to H.-Q. Zhang and the HSOS team for their hospitality in Beijing and at the Huairou station and for making their data available. Hα images from BBSO (New Jersey Institute of Technology, NJIT) were provided with the kind assistance of V. Yurchyshyn. Those from the Learmonth Observatory (part of SOON operated by the U.S. Air Force) were provided by SOONSPOT with the kind assistance of A. Kiplinger. *Wind* and *Ulysses* radio data were provided by the "Centre de Données de la Physique des Plasmas" (CDPP). We gratefully acknowledge the open-data policies of *GOES*, *RHESSI* (NASA small explorer mission), NoRH (operated by the Nobeyama Solar Radio Observatory, NAOJ/NINS), and OVSA (NJIT).

REFERENCES

Acton, L. W., et al. 1992, PASJ, 44, L71
Ai, G., & Hu, Y. 1986, Publ. Beijing Astron. Obs., 8, 1

Aschwanden, M. J. 2004, Physics of the Solar Corona (Berlin: Springer)
Battaglia, M., Grigis, P. C., & Benz, A. O. 2005, A&A, 439, 737
Bonnin, X., Hoang, S., & Maksimovic, M. 2008, A&A, 489, 419
Bougeret, J., et al. 1995, Space Sci. Rev., 71, 231
Christe, S., Krucker, S., & Lin, R. P. 2008, ApJ, 680, L149
Coffey, H. E., & Lincoln, J. V. 1979, BAAS, 11, 435
Denker, C., Johannesson, A., Marquette, W., Goode, P. R., Wang, H., & Zirin, H. 1999, Sol. Phys., 184, 87
Edwin, P. M., & Roberts, B. 1983, Sol. Phys., 88, 179
Foullon, C., Verwichte, E., Nakariakov, V. M., & Fletcher, L. 2005, A&A, 440, L59 (F05)
Fu, Q., Qin, Z., Ji, H., & Pei, L. 1995, Sol. Phys., 160, 97
Fu, Q., et al. 2004, Sol. Phys., 222, 167
Gary, D. E., & Hurford, G. J. 1990, ApJ, 361, 290
Hanser, F. A., & Sellers, F. B. 1996, Proc. SPIE, 2812, 344
Harra, L. K., Matthews, S. A., & van Driel-Gesztelyi, L. 2003, ApJ, 598, L59
Holman, G. D. 2003, ApJ, 586, 606
Hori, K., Ichimoto, K., & Sakurai, T. 2007, in ASP Conf. Ser. 369, New Solar Physics with Solar-B Mission, ed. K. Shibata, S. Nagata, & T. Sakurai (San Francisco, CA: ASP), 213
Hori, K., Ichimoto, K., Sakurai, T., Sano, I., & Nishino, Y. 2005, ApJ, 618, 1001
Hurford, G. J., Read, R. B., & Zirin, H. 1984, Sol. Phys., 94, 413
Hurford, G. J., et al. 2002, Sol. Phys., 210, 61
Kahler, S. 1977, ApJ, 214, 891
Karlický, M. 2004, A&A, 417, 325
Khan, J. I., & Hudson, H. S. 2000, Geophys. Res. Lett., 27, 1083
Khan, J. I., Vilmer, N., Saint-Hilaire, P., & Benz, A. O. 2002, A&A, 388, 363
Kiplinger, A. L. 1998, http://www.swpc.noaa.gov/solcoord/soonspotinfo.html
Kliem, B., Dammasch, I. E., Curdt, W., & Wilhelm, K. 2002, ApJ, 568, L61
Kliem, B., Karlický, M., & Benz, A. O. 2000, A&A, 360, 715
Kołomański, S., & Karlický, M. 2007, A&A, 475, 685
Lehtinen, N. J., Pohjolainen, S., Karlický, M., Aurass, H., & Otruba, W. 2005, A&A, 442, 1049
Li, Y. P., & Gan, W. Q. 2008, Sol. Phys., 247, 77
Lin, R. P., et al. 2002, Sol. Phys., 210, 3
Milligan, R. O., McAteer, R. T. J., Dennis, B. R., & Young, C. A. 2010, ApJ, 713, 1292
Nakajima, H., et al. 1994, Proc. IEEE, 82, 705
Nakariakov, V. M., Foullon, C., Myagkova, I. N., & Inglis, A. R. 2010, ApJ, 708, L47
Nakariakov, V. M., Foullon, C., Verwichte, E., & Young, N. P. 2006, A&A, 452, 343
Nakariakov, V. M., & Melnikov, V. F. 2006, A&A, 446, 1151
Nakariakov, V. M., Melnikov, V. F., & Reznikova, V. E. 2003, A&A, 412, L7
Nakariakov, V. M., Ofman, L., Deluca, E. E., Roberts, B., & Davila, J. M. 1999, Science, 285, 862
Ofman, L., & Sui, L. 2006, ApJ, 644, L149
Ohyama, M., & Shibata, K. 1998, ApJ, 499, 934
Phillips, K. J. H. 2004, ApJ, 605, 921
Reiner, M. J., Fainberg, J., Kaiser, M. L., & Stone, R. G. 1998, J. Geophys. Res., 103, 1923
Roberts, B., Edwin, P. M., & Benz, A. O. 1983, Nature, 305, 688
Roberts, B., Edwin, P. M., & Benz, A. O. 1984, ApJ, 279, 857
Starck, J.-L., & Murtagh, F. 2002, Astronomical Image and Data Analysis (Astronomical and Astrophysics Library; Berlin: Springer)
Stone, R. G., et al. 1992, A&AS, 92, 291
Sui, L., & Holman, G. D. 2003, ApJ, 596, L251
Sui, L., Holman, G. D., & Dennis, B. R. 2004, ApJ, 612, 546
Sui, L., Holman, G. D., White, S. M., & Zhang, J. 2005, ApJ, 633, 1175
Švestka, Z., Fárník, F., Hudson, H. S., Uchida, Y., Hick, P., & Lemen, J. R. 1995, Sol. Phys., 161, 331
Sylwester, J., Sylwester, B., & Phillips, K. J. H. 2008, ApJ, 681, L117
Veronig, A. M., Karlický, M., Vršnak, B., Temmer, M., Magdalenić, J., Dennis, B. R., Otruba, W., & Pötzi, W. 2006, A&A, 446, 675
Verwichte, E., Aschwanden, M. J., Van Doorsselaere, T., Foullon, C., & Nakariakov, V. M. 2009, ApJ, 698, 397
Verwichte, E., Foullon, C., & Van Doorsselaere, T. 2010, ApJ, 717, 458
White, S. 2004, in Solar and Space Weather Radiophysics, ed. D. Gary & C. Keller (Astrophysics and Space Science Library, Vol. 314; Dordrecht: Springer), 89
White, S. M., Thomas, R. J., & Schwartz, R. A. 2005, Sol. Phys., 227, 231
Zimovets, I. V., & Struminsky, A. B. 2009, Sol. Phys., 258, 69
Zimovets, I. V., & Struminsky, A. B. 2010, Sol. Phys., 263, 163